Thermal Decomposition of Mixed Calcium Oxalate Hydrates - Kinetic Deconvolution of Complex Heterogeneous Processes

Roman Svoboda,*[1] Zuzana Olmrová Zmrhalová[2], Dušan Galusek[3], Daniela Brandová[1], Jozef Chovanec[3]

[1]*University of Pardubice, Faculty of Chemical Technology, Department of Physical Chemistry, Studentska 573, 532 10 Pardubice, Czech Republic.*
[2]*University of Pardubice, Joint Laboratory of Solid State Chemistry, Studentska 84, 532 10 Pardubice, Czech Republic*
[3]*Vitrum Laugaricio - Joint Glass Center of IIC SAS, TnUAD, FChPT STU, Centre for functional and surface functionalized glass, Študentsská 2, 91150 Trenčín, Slovakia*

Abstract

Differential scanning calorimetry (DSC), thermogravimetry (TG) and in-situ XRD were used to study dehydration and consequent decomposition reactions of mixed calcium oxalate hydrates. As the complex dehydration kinetics exhibited certain trends with respect to the applied heating rate, the modified multivariate kinetic analysis approach (based on averaged curve-by-curve optimizations) was employed to obtain full kinetic description of the data. Šesták-Berggren equation was used to model the two consequent dehydration reactions. Good agreement was found between the kinetic parameters calculated from the DSC and TG data – approximate values of activation energies were 68 and 81 kJ·mol^{-1} for the trihydrate→monohydrate and monohydrate→anhydride transformations, respectively. Procedural methodology was developed to predict both, dehydration kinetics and hydrate content ratio. For the calcium oxalate decomposition the TG technique provided very precise single-step prediction with activation energy 180 kJ·mol^{-1}. DSC on the other hand provided complex information on joint decomposition and carbon monoxide oxidation reactions – proposed reaction mechanism includes completion of two reaction paths composed from

* Corresponding author: Tel.: +420 466 037 346; E-mail address: roman.svoboda@upce.cz

consequent chemical reactions. Mechanistic view of the complex reaction path is discussed in terms of diffusion barrier limiting the oxidation step.

Keywords: oxalate hydrates, dehydration, decomposition, reaction kinetics, DSC, TG

1. Introduction

Hydrated calcium oxalate ($CaC_2O_4 . xH_2O$) commonly occurs as whewellite (monohydrate, COM) and weddellite (dihydrate, COD), rarely also in the trihydrated form – caoxite, COT. [1-3] Industrial usage of oxalate hydrates includes e.g. thermochemical energy storage [4] (the reversible chemical reaction anhydride CaOx↔COM is utilized), synthesis of superconducting multicomponent oxides [5, 6], preparation of high purity titanates, stannates, ferrites and zirconates [7 - 9] or separation of rare earth elements from raw ores by co-precipitation [10]. However, major importance of these minerals dwells in the fact that they are the main crystalline components of human urinary stones. [11 - 13] As approximately 20 % of world population [14] suffer from the urinary stone disease, significant effort was put into investigation of the processes and mechanisms behind the formation of the urinary stones: formation of the thermodynamically stable COM was found to be conditioned by high oxalate contents in urine (caused either by inflammatory bowel disease [15], Golding Bird's disease [16] or excess intake of oxalates from food [17 - 19]), occurrence of COD is then often associated with high $Ca^{2+}/C_2O_4^{2-}$ ratio (resulting either from excessive secretion of calcium into urine or from excessive intestinal calcium absorption) [20, 21]. In compliance with these efforts number of microscopic crystal growth [22 - 32] and dissolution [33 - 37] studies were performed to determine the formation/destruction rates of calcium oxalate in controlled environment. These studies can be utilized in research focused on prevention of urinary stones genesis. Nonetheless, as the soluble impurities are the predominate factor for nucleation and crystal growth rates of oxalate hydrates [38 - 41], the true predictions of

urinary stone formations are rather unreliable. Therefore the clinical routine needs to adopt the analytic approach based on the thermal analysis of the urinary stones. In this regard significant amount of studies were performed, mainly for the anhydride, COM and COD. However, many of these studies [42 - 47] were qualitative, aimed at characterization of the samples and determination of the characteristic temperatures and dehydration/decomposition enthalpies, rather than report of full kinetic studies based on which a prediction of the process course could be made. Several such detailed studies are listed below.

Masuda et al. [48] studied, thermogravimetrically, kinetics of thermal dehydration of COM under the flow on nitrogen (50 $cm^3 \cdot min^{-1}$) and in static air. They adopted an approach, where temperature-variable kinetic parameters were used to describe an overlap of two involved processes. The initial slow mass decrease was described by the first order reaction model (F1) [49] with the following variation of kinetic parameters: activation energy $E = 77.5 – 86.0\ kJ \cdot mol^{-1}$ and pre-exponential factor $\log(A \cdot s^{-1}) = 8.50 – 9.39$; the process was associated with external diffusion of water molecules eliminated from the sample surface. The main dehydration process was described by the two-dimensional phase boundary reaction (R2) [49] with the following parameters: activation energy $E = 119 – 189\ kJ \cdot mol^{-1}$ and pre-exponential factor $\log(A \cdot s^{-1}) = 14.05 – 22.66$. The onsets of the main dehydration process were determined to be 118 and 128 °C in nitrogen and air, respectively (measured at heating rate $q^+ = 2.5\ °C \cdot min^{-1}$).

Kutaish et al. [50] used thermogravimetry to study dehydration and decomposition of oxalate hydrates (COMs and CODs) prepared by various synthesis routes. As expected, the activation energy for the dehydration process varied significantly in dependence on the given synthesis route – from 69 to 115 $kJ \cdot mol^{-1}$. Surprisingly, also the consequent decomposition of oxalate to carbonate exhibited massive variance in the activation energy of the process – from 180 to 290 $kJ \cdot mol^{-1}$, which indicates that during dehydration the calcium oxalate crystallites

retain the specific morphology gained during the synthesis. Both reaction stages (dehydration and decomposition) were described in terms of the first order kinetics and showed a compensation effect (linearity of the E-A dependence obtained by gathering data from multiple samples).

Similar study was published by Anderson et al. [51], who performed a round robin test on kinetic evaluation of COM dehydration and decomposition in 13 European thermogravimetric laboratories. The variances in activation energy E for the dehydration step were 64 – 130 $kJ \cdot mol^{-1}$ (air, independent evaluation of A for each measurement), 94 – 107 $kJ \cdot mol^{-1}$ (air, compensation for A [52, 53]), 78 – 104 $kJ \cdot mol^{-1}$ (inert gas, independent evaluation of A for each measurement), 85 – 98 $kJ \cdot mol^{-1}$ (air, compensation for A). The variances in activation energy E for the decomposition to carbonate were 223 – 310 $kJ \cdot mol^{-1}$ (air, independent evaluation of A for each measurement), 253 – 320 $kJ \cdot mol^{-1}$ (air, compensation for A), 213 – 285 $kJ \cdot mol^{-1}$ (inert gas, independent evaluation of A for each measurement), 229 – 291 $kJ \cdot mol^{-1}$ (air, compensation for A).

Bhatt et al. [54] studied dehydration and decomposition of COM-based urinary calculi by using thermogravimetry. They obtained E = 40.9 $kJ \cdot mol^{-1}$ and order of the reaction (with the n-th order reaction model [49]) n = 0.71 for the dehydration, and E = 51.4 $kJ \cdot mol^{-1}$ and order of the reaction n = 0.38 for the decomposition to carbonate. Honcová et al. [55] studied dehydration of COT via differential scanning calorimetry (DSC) – the two overlapping peaks were described with the following kinetic parameters: activation energies equal to 69 and 83 $kJ \cdot mol^{-1}$ for the first and second endothermal effect, respectively; reaction orders equal to 0.5 for both dehydration steps. Budrugeac et al. [56] reported activation energy for thermogravimetric dehydration of COM to be 125 $kJ \cdot mol^{-1}$ in the range of degree of conversion (0 – 15 %) and 94 $kJ \cdot mol^{-1}$ for the range (20 – 70 %). Nishikawa et al. [57]

reported the following activation energies for COT dehydration studied by thermogravimetry: 87.9 and 105.3 kJ·mol^{-1} for the first and second dehydration steps, respectively.

Several authors have also paired certain thermoanalytical techniques to provide a complex explanation for the reaction mechanism. Kaloustian et al. [58, 59] have shown a good correlation between the DSC and DTG results in a study of 33 urinary stones (mixed COM and COD contents) – the temperatures of DSC and DTG peak maxima as well as number of hydrate waters determined by both techniques were matched with correlation coefficient 0.99. McGhie [60] reported exceptionally good correlation between the DTG and MS (quadrupole mass spectrometer coupled with DTA-TG instrument) results on full 3-step decomposition route of COM (i.e. dehydration followed by decomposition to carbonate followed by decomposition to oxide). Although no kinetic calculations were performed, figures depicting overlay of the DTG and MS data showed complete match for the decomposition to oxide and very good match for the decomposition to carbonate. MS resolution for the dehydration was quite poor but for this step very good correlation between the DTA and DTG signals was found. Frost et al. [61] have reported similar type of qualitative results for coupled TG-MS measurements of COM. In case of this study very good correlations (based again on the peak shapes similarities) were obtained for the dehydration step and for the decomposition to oxide.

As is apparent, a significant variety of outcomes has been obtained regarding the absolute values of activation energy, pre-exponential factor and kinetic model exponent; even the round robin test [51] performed in renowned laboratories did not result in stipulation of a single set of kinetic parameters for the exactly same provided compound (COM). It seems that the clinical studies of urinary stones (generally complex mixtures of various oxalate hydrates) will greatly benefit from employment of multiple thermoanalytical techniques, where the paired results would not only lead to unambiguous and more accurate conclusions

but also to more precise clinical models and predictions. However, up to this date there are only very few studies (most being rather qualitative) performed by multiple TA techniques on the same oxalate material in the same laboratory.

Motivation for the present article is to establish a methodology for kinetic modeling of complex multi-phase kinetics of mixed oxalate hydrates occurring in urinary stones. The approach will be based on kinetic deconvolution of DSC and TG data-curves recorded under similar conditions. Synthesis-formed mixture of tri- and mono-hydrated calcium oxalates will be used as a model material.

2. Kinetic theory and modeling

The kinetics of physico-chemical transformations in solid phase is described by formal kinetic equation derived for calculation of the rate of conversion [62]:

$$d\alpha/dt = A \cdot e^{-E/RT} \cdot f(\alpha) = \Phi/\Delta H \quad (1)$$

where α is the degree of conversion, A is the pre-exponential factor, E is the apparent activation energy of the process, $f(\alpha)$ is a substitute for a kinetic model, Φ is the DSC heat flow and ΔH is the enthalpy change associated with the given kinetic process. In the present work the original Kissinger [63] method and isoconversional modified Kissinger-Akahira-Sunose (KAS) method [64] will be used – see Eqs. 2 and 3.

$$\ln\left(\frac{q^+}{T_p^2}\right) = -\frac{E}{RT_p} + const. \quad (2)$$

$$\ln\left(\frac{q^+}{T_\alpha^{1.92}}\right) = -1.008\frac{E}{RT_\alpha} + const. \quad (3)$$

The model-based part of kinetic analysis (suggestion of the appropriate model function $f(\alpha)$ and determination of the potential kinetic exponents of the model) will be in the present work solved via multivariate kinetic analysis (MKA) [65] – see Eqs. 4 and 5.

$$RSS = \sum_{j=1}^{n} \sum_{k=First_j}^{Last_j} w_{j,k} \left(Y\exp_{j,k} - Ycal_{j,k}\right)^2 \quad (4)$$

$$w_j = \frac{1}{\left|\left[d\alpha/dt\right]_{\max}\right|_j + \left|\left[d\alpha/dt\right]_{\min}\right|_j} \quad (5)$$

where *RSS* is the sum of squared residui, *n* is number of measurements, *j* is index of the given measurement, $First_j$ is the index of the first point of the given curve, $Last_j$ is the index of the last point of the given curve, $Yexp_{j,k}$ is the experimental value of the point *k* of curve *j*, $Ycal_{j,k}$ is the calculated value of the point *k* of curve *j* and w_j is weighting factor for curve *j*. The software used for the kinetic evaluation of the present data was the Thermokinetics 3.1, Netzsch [66].

In the present work the following kinetic models will be considered: nth order reaction model (Eq. 6) [67], nucleation-growth Johnson-Mehl-Avrami model (Eq. 7) [68-70], autocatalytic Šesták-Berggren model (Eq. 8; similar to the expanded Prout-Tompkins model) [62] and nth order reaction model with autocatalysis (Eq. 9) [66].

$$f(\alpha) = (1-\alpha)^n \quad (6)$$

$$f(\alpha) = m(1-\alpha)[-\ln(1-\alpha)]^{1-(1/m)} \quad (7)$$

$$f(\alpha) = \alpha^M (1-\alpha)^N \quad (8)$$

$$f(\alpha) = (1-\alpha)^n (1-K\alpha) \quad (9)$$

Note that each of the above-listed kinetic models includes certain kinetic exponent(s) responsible for the actual shape of the DSC peak.

3. Experimental

Synthesis of the mixed calcium oxalate hydrates was performed based on the reaction of oxalic acid and calcium chloride. The reaction conditions were set up in accordance with [71], where it was pointed out that COT precipitates from high ionic strength solutions. In addition to ionic strength the precipitation products are determined by pH and temperature. [55] The following parameters were used for the present synthesis: 0.2 mol·dm^{-3} $CaCl_2$ solution, 0.5 mol·dm^{-3} $H_2C_2O_4$ solution (in 10 % surplus; introduced into the chloride solution

via incremental additions), 12 °C, pH in the range 1.1 – 1.3 (maintained via drop-size introductions of HCl). The precipitated crystallites were filtered and washed with distilled water, ethanol and ether. The crystallites were kept in a dry environment at 5 °C.

The DSC measurements were realized by using heat-flow differential scanning calorimeter Q2000 (TA Instruments) equipped with an autosampler, RCS90 cooling accessory, and T-zero technology. The instrument was calibrated using In, Zn, and H_2O; dry N_2 was used as purge gas at a flow rate of 50 $cm^3 \cdot min^{-1}$. The sample masses of approx. 3 mg were accurately weighted into low-mass T-zero pans (no lid was used in order for the dehydration/decomposition products to by freely removed by the purge gas). The dehydration/decomposition kinetics were measured by means of simple heating scans performed at selected heating rates q^+ = 0.5, 1, 2, 3, 5, 7, 10, 15, 20, 30 and 50 $°C \cdot min^{-1}$ from -20 to 300 °C.

Thermogravimetric analysis of the samples was carried out by PerkinElmer Pyris 1 TGA with high temperature furnace in a flowing nitrogen atmosphere (20 $cm^3 \cdot min^{-1}$). The samples were heated in a ceramic crucible from laboratory temperature to 550 °C at different heating rates: 0.5, 1, 2, 3, 5, 7, 10, 20, 30, 50 $°Cmin^{-1}$. Used sample masses were approx. 9 mg. Instrumental accuracy of temperature measurements was declared to be 5 °C. However, both TGA and DSC measurements were very well reproducible, as confirmed by repeated experiments at selected heating rates. The reason for including the wide range of q^+ in both DSC and TG experiments was to map in detail the kinetic behavior of the observed processes and to identify its potential changes associated with the thermal lags and heat/mass transfer phenomena. Wide range of applied heating rates also allows for better predictions of the described kinetics, and it can be very beneficial for revealing mutually dependent kinetic processes (as will be shown in section 4.3.).

Morphology of the formed crystallites was checked by scanning electron microscopy (SEM) JEOL JSM 7500F in the field-emission setup. Structural information was obtained by X-ray powder diffraction (XRD) using Panalytical Empyrean DY1098 diffractometer, operated at 40kV and 45 mA with Cu Kα radiation (λ = 0.15405 nm). The data were acquired over a 2θ range of 10 – 50° (step size 0.05 °). In addition to the standard XRD characterization patterns (obtained at laboratory temperature), the in-situ XRD heating scans were performed for the selected vanadium contents in a step-wise process: heating rate during non-isothermal segments was 1 °C·min^{-1}, duration of isothermal segments during which the patterns were collected was 65 s, temperature step between collecting the individual patterns was 2 °C. The data were evaluated using the Panalytical HighScore Plus software package with the PDF4+ database. In addition, Raman shift signals were measured using the DXR2 Raman microscope (Nicolet, Thermo Fisher Scientific), utilizing the 785 nm excitation diode laser (30 mW, laser spot size 1.6 μm, 90 scans → 10 s each) and CCD detector.

4. Results and discussion

4.1. Sample characterization

Typical DSC and TG curves obtained at heating rate 5 °C·min^{-1} for the as-prepared mixture of calcium oxalate hydrates are shown in Fig. 1A. As evidenced by the corresponding TG steps, mass of the sample decreases first in the 50 – 150 °C temperature range due to the loss of hydrate water and then in the 300 – 450 °C temperature range due to the decomposition of anhydrous oxalate and release of CO – see Eqs. 10 and 11, respectively:

$$CaC_2O_4 \cdot nH_2O \rightarrow CaC_2O_4 + nH_2O \quad (10)$$

$$CaC_2O_4 \rightarrow CaCO_3 + CO \quad (11)$$

Similar effects are present also on the DSC curve, first two endothermal peaks corresponding to the loss of hydrate water and at 450 °C an exothermal peak associated with the

decomposition. Note that whereas the dehydration effects show very similar kinetics (position on the temperature axis and general shape of the kinetic peaks) for both DSC and derivative TG (DTG) data-curves, the decomposition peaks are significantly different in shape and (more importantly) temperature position – this disparity will be discussed later in section 4.3.

The release of hydrate water proceeds evidently in two steps. The mass losses determined by TG (see the red curve in Fig. 1A) indicate that the overall formula corresponds to the content of ~ 1.5 H_2O: first dehydration step exhibits 5.9 % mass loss (theory predicts 5.8 %), the second dehydration step (COM→anhydride) exhibits 12.2 % mass loss (theory predicts 11.6 %) and the third, decomposition step exhibits 17 % mass loss (theory predicts 18 %) – the agreement of experimental and theoretical mass loss values for the decomposition step essentially confirm the correct calibration of the TG instrument as well as the correct experimental setup/treatment. Considering the synthesis route, it is safe to assume that a mixture of COM and COT was prepared. In order to confirm this assumption, XRD, Raman spectroscopy and SEM techniques were employed.

In Fig. 1B the XRD diffraction patterns for as-prepared material and sample heated to 90 °C in DSC (just above the first dehydration) are displayed. The enclosed JCPDS patterns [72] of COT (00-020-0231) and COM (04-014-9825) clearly show presence of both hydrates (COT and COM) in the as-prepared material, whereas after the first dehydration step only COM is identified. The same two samples were also explored via Raman spectroscopy; in Fig. 1C the two Raman spectra are compared - the inset zooms in on one of the most crucial spectral regions. For COT the most prominent spectral bands are assigned as follows: 507 cm^{-1} O-C-O in-plane asymmetric bend, 867 cm^{-1} C-C symmetric stretch, 912 cm^{-1} O-C-O in-plane symmetric bend, 1472 cm^{-1} C-O symmetric stretch. [73] In case of COM the most prominent bands are: 503 cm^{-1} O-C-O in-plane asymmetric bend, 867 cm^{-1} C-C symmetric stretch, 896 cm^{-1} O-C-O in-plane symmetric bend, 1463 and 1490 cm^{-1} C-O symmetric

stretch, 1629 cm^{-1} C-O asymmetric stretch. [61, 74 - 76] Schematic illustration of these vibrations is depicted in Fig. 1. As is apparent from Fig. 1C, the as prepared material shows evidence of COT (additional bands at 912 and 1472 cm^{-1}) in addition to the standard COM spectrum. Lastly, the SEM micrograph of the as-prepared material (see Fig. 1) clearly displays three types of crystallites – large crackled elongated sword-shape COT crystals, medium-sized prismatic COM crystals and aggregates of small COM dendrites and elliptic cylinder crystals. No evidence of bipyramidal COD crystallites was found.

The information provided by XRD, Raman spectroscopy and SEM prove that the synthesized material is a mixture of COT and COM. With this knowledge the DSC data in Fig. 1A can be quantitatively interpreted. The DSC curve shows two distinct dehydration steps; similar two steps were reported in the DSC studies of COT [55, 57] but with reverse proportional magnitude. In [55] the enthalpies associated with the first and second step were approx. 546 (attributed to the loss of 2 water molecules, i.e. COT→COM) and 312 $J \cdot g^{-1}$ (attributed to the loss of 1 water molecule, i.e. COM→anhydride), respectively; in [57] the two respective enthalpies were 573 and 289 $J \cdot g^{-1}$. In the present data, the first and second dehydration steps exhibit enthalpies 106 and 320 $J \cdot g^{-1}$, respectively. In order to compare the dehydration enthalpy values, the data have to be normalized with respect to the mass of the same material COM (all the above-listed values are normalized on the overall sample mass, where the composition differs). For the second dehydration step (COM→anhydride) this transformation gives values 389 $J \cdot g_{\_COM}^{-1}$ [55], 360 $J \cdot g_{\_COM}^{-1}$ [57] and 340 $J \cdot g_{\_COM}^{-1}$ (present data), which is in reasonable agreement – the differences may be caused by slightly different dehydration enthalpies being associated with the particular COM morphologies (prisms, dendrites, elliptical cylinders). Similar calculation gives 681 $J \cdot g_{\_COM}^{-1}$ [55], 713 $J \cdot g_{\_COM}^{-1}$ [57] and 112 $J \cdot g_{\_COM}^{-1}$ (present data) for the first dehydration step. Considering that a mixture of COT and COM was prepared during the present synthesis, the TG data suggest that approx.

¼ of the initial material was in the trihydrate form – surplus 0.5 H_2O (additive to the monohydrate) determined for present data versus 2 H_2O for full COT. However, from comparison of the DSC enthalpies one would assume that only approx. 1/6 of the initial material is in the COT form. This discrepancy may be caused by the seeding effect – number of the small COM crystallites appears to grow directly from the surface of the COT crystals or are partially embedded in it (see Fig. 1), which may decrease the energy needed for the initial dehydration. This issue will be further discussed in section 4.2.

4.2. Dehydration kinetics

Multivariate kinetic analysis (Eqs. 4 and 5) was used to evaluate the dehydration kinetics of the prepared COM/COT co-crystals. In Fig. 2A the full set of DSC data (already corrected for the baseline subtraction) is depicted. In order to reduce the number of optimized kinetic parameters, the methods of model-free kinetic analysis were applied in the first step to determine the apparent activation energy. As the two dehydration sub-processes are only partially overlapped, it was possible to apply the Kissinger method (which is based on the temperatures corresponding to the DSC peak maxima; see Eq. 2) – the Kissinger plot for the two sub-processes is shown in Fig. 2B. Both dependences are fairly linear (with only slight curvature present at highest heating rates), indicating that activation energy is independent from the inherent experimental conditions (temperature/heating rate). [77] In addition to the Kissinger method the isoconversional KAS method (Eq. 3) was used, providing the dependence of E on α – as displayed in Fig. 2B. As is apparent, the E-α data show reasonable agreement with the E values determined for the two sub-processes via the Kissinger method (68.6 and 81.5 $kJ \cdot mol^{-1}$, respectively; indicated by red dashed lines in Fig. 2B).

However, even with pre-set E values the simultaneous MKA non-linear optimization of all data-curves resulted in a relatively poor fit with $r^2 = 0.981$ due to the change of the peak

shape (q^+-dependent model-free kinetics). Note the slightly more skewed peaks obtained at low q^+ (see Fig. 2A). Therefore a modified approach has been adopted, based on single curve optimizations with fixed E_1 and E_2 values (subscripts correspond to the particular sub-processes) obtained from the full dataset of measured DSC curves. In this way the consistency of the results with respect to the inherent experimental conditions (T, q^+) can be checked (and averaged in case of acceptable level of similarity) and any inconsistences can be interpreted. In Fig. 2C the dehydration enthalpies determined by means of MKA for each particular DSC curve are displayed – the overall dehydration enthalpy and the partial contributions corresponding to the two sub-processes. In addition, the data (represented by the blue dashed lines) obtained by simultaneous optimization of all DSC curves are shown in Fig. 2C. The comparison shows that the data on dehydration enthalpy are very consistent and reliable and that both ways of ΔH_1 and ΔH_2 determination (either simultaneous optimization of all curves or averaged results of single-curve optimizations) are equivalent. This is by the way very advantageous with respect to the determination of proportional representation of particular hydrates (as needed e.g. for the kidney stone studies) because the much simpler approach (simultaneous optimization of all data) provides equally good results as the more complicated way based on the single-curve fits.

Contrary to the dehydration enthalpies, the model-based part of the MKA evaluation was found to be significantly q^+-dependent. Best descriptive effectivity was achieved for overlap of two autocatalytic Šesták-Berggren kinetics (Eq. 8). As is apparent from Fig. 2D, the kinetics of the first sub-process (transition from COT to COM; black-based points in Fig. 2D) is fairly invariant with respect to q^+. On the other hand, evolution of the Šesták-Berggren kinetic exponents determined for the second kinetic sub-process massively changes with q^+: the exponent N_2 responsible for skew of the ascending side of the kinetic peak largely increases with q^+. It is also apparent that in case of N_2 the simultaneous MKA optimization

resulted in a completely incorrect value (upper red dashed line in Fig. 2D), largely deviated from any true values obtained by the curve-by-curve optimization approach. Apart from the Šesták-Berggren equations the other kinetic models listed in Section 2 were also tested: almost comparable results ($r^2 = 0.9806$ for the simultaneous optimization and equally good fits, i.e. ~ 0.997, for the averaged curve-by-curve approach) were achieved for the double n^{th} order reaction model with autocatalysis (Eq. 9), which is usually very close or even surpasses in performance the Šesták-Berggren model; unacceptable quality of description was obtained for the double n^{th} order reaction model ($r^2 = 0.978$ and 0.980 for the respective simultaneous and curve-by-curve approaches) and for the Johnson-Mehl-Avrami model ($r^2 = 0.985$ and 0.986 for the respective simultaneous and curve-by-curve approaches). It should be also noted that in case of open systems the heat/mass transfer phenomena may influence the apparent kinetics. In case of the present DSC dehydration measurements this might be the cause for the increase of parameter N_2 with increasing q^+ (see Fig. 2D). However, since the enthalpies of the overall dehydration process as well as sub-processes do not change with q^+ (see Fig. 2C), the more probable reason for the deviation of the kinetic behavior is the possible thermal lag within the sample associated with the heat propagation at high q^+.

Regarding the exact type of kinetic complexity, similar correlation coefficients were obtained for the consequent and independent model chemical reactions, which both are represented by the mathematically similar sets of equations. The consequent reactions give:

$$\frac{da}{dt} = -A_1 \cdot \exp\left(-\frac{E_1}{RT}\right).f_1(a,b) \tag{12}$$

$$\frac{db}{dt} = A_1 \cdot \exp\left(-\frac{E_1}{RT}\right).f_1(a,b) - A_2 \cdot \exp\left(-\frac{E_2}{RT}\right).f_2(b,c) \tag{13}$$

$$a = \frac{[COT]}{[COT]_0} \qquad b = \frac{[COM]}{[COM]_0} \qquad c = \frac{[CaOx]}{[CaOx]_0} \tag{14 a,b,c}$$

and the independent reactions are described via:

$$\frac{da}{dt} = -A_1 \cdot \exp\left(-\frac{E_1}{RT}\right).f_1(a,b) \tag{15}$$

$$b = 1 - a \qquad a = \frac{[COT]}{[COT]_0} \qquad b = \frac{[COM]}{[COM]_0} \qquad (16\ a,b,c)$$

$$\frac{dc}{dt} = -A_2 \cdot \exp\left(-\frac{E_2}{RT}\right) \cdot f_2(c,d) \qquad (17)$$

$$d = 1 - c \qquad c = \frac{[COM]}{[COM]_0} \qquad d = \frac{[CaOx]}{[CaOx]_0} \qquad (18\ a,b,c)$$

where subscript "0" denotes the initial concentrations/amounts of the given hydrate form. Formally, the two-step dehydration COT → COM → CaOx is a consequent reaction; however as the SEM micrographs have shown (see Fig. 1) both hydrates coexist in the initial material and due to the possible seeding effects the COM originating from COT dehydration may exhibit slightly different dehydration kinetics in comparison with the COM single crystals and co-crystals being present in the as-prepared sample. In fact the complex kinetic mechanism should therefore be in the first approximation composed of a combination of independent consequent and single process reactions. However, the non-linear optimization employing this improved reaction scheme did not improve the correlation coefficients significantly – the major issue was still the q^+-dependent kinetics of the COM → CaOx reaction step. This shows that the simplified reaction step (employing either consequent or independent reactions) is acceptable for solving the dehydration kinetics of calcium oxalate hydrates.

In addition to the DSC measurements, thermogravimetry was employed to study the dehydration kinetics of the prepared mixture of oxalates. The complete set of obtained TG data-curves is displayed in Fig. 3A (the inset shows measurements at lower heating rates). Similar approach to evaluation of dehydration kinetics as in case of the DSC data was adopted. The results from Kissinger and modified KAS methods are shown in Fig. 3B – significantly more curved Kissinger plot dependences are probably a consequence of triple sample masses associated with larger thermal gradients evolving at higher heating rates. Nonetheless, the activation energies determined by Kissinger method (66.7 and 82.1 $kJ \cdot mol^{-1}$ for the two respective sub-processes) are very close to those determined from the DSC data

(68.6 and 81.5 kJ·mol^{-1}). The isoconversional KAS method results in general agree with the E values provided by the Kissinger method, but exhibit significantly higher scatter compared to the similar evaluation performed on the DSC data (see Fig. 2B).

Whereas the activation energies for the two sub-processes obtained based on both DSC and TG data were very similar, slightly different situation arose in case of the model-based analysis. Fig. 3C compares the values of Šesták-Berggren kinetic exponents for the two sub-processes, ratio coefficient I (which is defined as the percent contribution of the first sub-process to the overall complex signal, i.e. ratio between dehydration enthalpies $\Delta H_1/\Delta H$ in case of DSC data and ratio between mass losses $\Delta m_1/\Delta m$ in case of TG data) and correlation coefficients r^2 for DSC and TG results obtained by the two approaches (simultaneous optimization of all curves vs. averaged curve-by-curve fits). Regarding the kinetic exponents, in case of the second kinetic peak (COM→CaOx) a reasonable agreement occurs between all results, the data for the first kinetic peak (COT→COM) are more scattered – mainly the TG results. In general, the two optimization approaches exhibit better agreement in case of the differential (DSC) data compared to the integral (TG) data. It should be however noted that certain role in the distortion of the evaluated model-based kinetics is also played by the heat/mass transfer phenomena, which are significantly larger (due to the triple-size sample masses) in case of the TG measurements. Negligible difference is then shown in case of the ratio coefficient I, where both approaches and techniques provide very similar conclusions. The most important findings are those regarding the correlation coefficients r^2: optimization of the integral data in general provides significantly better r^2; the curve-by-curve optimization approach is needed to obtain reasonable r^2.

Lastly, in Fig. 3D the qualitative comparison of selected kinetic data provided by DSC, TG and in-situ XRD for the dehydration of COM/COT mixture is depicted. The DSC and TG experimental curves are transformed into α within the framework of standard kinetic

calculations, i.e. according the evolution of overall crystallization enthalpy ΔH and mass loss Δm. In case of the in-situ XRD data the degree of conversion was calculated from the loss of integral intensity in the 15.85 – 16.55 ° range, where a single COT diffraction line not overlapped with any COM signals is located. The absolute value of the XRD α-step was arbitrarily set to be 0.33 (in accordance with the α change corresponding to the COT→COM transformation obtained based on the TG data); note that COM and CaOx XRD patterns are very similar with overlapping diffraction lines, hence the second dehydration step could not be recognized via in-situ XRD. Whereas at higher heating rate the DSC and TG kinetics (shape of the α-T dependences) are fairly similar (see the inset in Fig. 3D), in case of low heating rates the kinetics significantly differ – both TG and XRD data show much faster (but temperature-delayed) COT→COM transition compared to the DSC data. This raises question of compatibility of various thermoanalytical signals under borderline conditions and reliability of such measurements: recording of the mass loss during the release of weakly bound water at low temperatures can be hindered e.g. by diffusion of the water vapor through the layered powder material (notice the significantly larger sample masses in case of TG) and also affected by the raw instrument capability of performing such low-temperature measurements (considering both temperature limitations of the instrument and development of thermal gradients within the sample leading to local changes of temperature). In case of the present XRD measurements the loss of the diffraction signals (diminution of the JCPDS00-020-0231 phase) is recorded, which a priori does not have to be directly proportional to the true α (contrary to the formation of crystalline phase from the amorphous matrix). In addition, calibration of temperature scale in cases of both TG and in-situ XRD is not as reliable as in case of the DSC instrument, which may cause certain shifts in temperature (especially on the borderline of the instrument temperature range).

If we compare the present dehydration data with literature, there is almost perfect agreement with E values determined by DSC published in [55] – differences are below 5 %. In case of dehydrations measured by TG there is significantly higher scatter in the published data. Thermogravimetric activation energy for the COT→COM process was actually reported only in [57] $E \approx 88$ kJ·mol^{-1} (versus present 67 kJ·mol^{-1}). On the other hand, thermogravimetry measurements of COM dehydration (COM→CaOx; the second step identified in case of the present study) are quite numerous, [48, 50, 51, 54, 56, 57] ranging from 45 to 190 kJ·mol^{-1}. Note however that the median for the reported E_{TG} values is around 90 kJ·mol^{-1}, which is in a good agreement with our results (82 kJ·mol^{-1}).

4.3. Decomposition kinetics

As shown in Fig. 1A, the anhydride calcium oxalate (CaOx) decomposes to calcium carbonate and carbon monoxide (see Eq. 11). Thermogravimetry indeed shows a single mass loss step as depicted in Fig. 4A. The multivariate kinetic analysis applied to the TG decomposition data showed remarkable similarity between the description qualities provided by the Šesták-Berggren model (Eq. 8; $r^2 = 0.99957$) and n^{th} order reaction model with autocatalysis (Eq. 9; $r^2 = 0.99969$). The MKA results for the Šesták-Berggren model were: E = 180.7 kJ·mol^{-1}, log(A/s^{-1}) = 11.61, M = 0.084 and N = 0.568. The MKA results for the n^{th} order autocatalytic model were: E = 180.4 kJ·mol^{-1}, log(A/s^{-1}) = 11.43, logK = 0.1664 and n = 0.860. The activation energies determined by MKA are in a good agreement with published data [48, 50]. In addition to the MKA, the Kissinger and modified KAS methods were also applied to the TG decomposition data – see Fig. 4B. Whereas the isoconversional KAS method (red points) gives very similar E values compared to the MKA results (red dashed line), the Kissinger plot (black points) results in significantly lower activation energy 147.7 ± 6 kJ·mol^{-1}. The slight curvature of the Kissinger plot responsible for the lower E

appears to indicate certain complexity of the decomposition reaction, probably associated with the different morphologies of the CaOx crystallites (originating either from the COT or COM crystals).

The above-mentioned assumption about the decomposition reaction complexity was indeed confirmed by the DSC measurements – while in case of the lower heating rates the decomposition peaks were relatively simple, exhibiting only a small shoulder (similar to that depicted in Fig. 1A), the data obtained at high q^+ started to show a very complicated kinetic behavior (see Fig. 4C). Literature survey has shown that somewhat similar behavior was described before: Gurrieri et al. [78] show via DTA (differential thermal analysis; predecessor of DSCs) that in highly pure N_2 atmosphere the decomposition proceeds as a single endothermic peak, in static air this reaction manifests as exothermic double-peak and in the flow of air only a single exothermic peak occurs; Gadalla [79] used DTA to study the CaOx decomposition in air and observed a complex kinetic reaction consisting from overlapping exothermic and endothermic processes (similar to our DSC data-curve obtained at 20 °C·min^{-1}). Both works attribute the endothermic peaks to the actual decomposition reaction (Eq. 11) and exothermal signals to the consequent oxidation of released carbon monoxide:

$$CO + O_2 \rightarrow CO_2 \tag{19}$$

but perform no further analysis of the complex decomposition process.

The MKA method was applied to explore the complex kinetics manifesting in case of the CaOx decomposition depicted in Fig. 4C. Firstly the appropriate kinetic mechanism needs to be developed. The transition from fully exothermal reaction to the endothermal initiation indicates a competition between two processes, where the difference in their activation energies leads to the preference of a particular process depending on applied heating rate. Furthermore, the strong exothermic signal following the endothermic decomposition increases proportionally to the endothermic area, which indicates that these two sub-processes are

linked (consequent reactions). Based on this analysis the reaction scheme depicted in Fig. 4C was proposed, based on the following sets of kinetic equations:

$$\frac{da}{dt} = -A_1 \cdot \exp\left(-\frac{E_1}{RT}\right).f_1(a,b) - A_2 \cdot \exp\left(-\frac{E_2}{RT}\right).f_2(a,c) \quad (20)$$

$$\frac{db}{dt} = A_1 \cdot \exp\left(-\frac{E_1}{RT}\right).f_1(a,b) \quad (21)$$

$$\frac{dc}{dt} = A_2 \cdot \exp\left(-\frac{E_2}{RT}\right).f_2(a,c) - A_3 \cdot \exp\left(-\frac{E_3}{RT}\right).f_3(c,d) \quad (22)$$

$$d = 1 - a - b - c \quad (23)$$

$$a = \frac{[CaOx]}{[CaOx]_0} \qquad b = \frac{[CO_2^I]}{[CO_2^I]_0} \qquad c = \frac{[CO^{II}]}{[CO^{II}]_0} \qquad d = \frac{[CO_2^{II}]}{[CO_2^{II}]_0} \quad (24\ a,b,cd)$$

where the upper indices I and II in Eqs. 24 b,c,d denote the two reaction routes as determined by the competing reaction step. The corresponding balance equation is:

$$\frac{d\alpha}{dt} = \delta_1 \cdot \frac{d(a \to b)}{dt} + \delta_2 \cdot \left(\delta_3 \cdot \frac{d(a \to c)}{dt} + (1-\delta_3) \cdot \frac{d(c \to d)}{dt}\right) \quad (25)$$

where $(x \to y)$ represents the heat flow on the path from reactant "x" to product "y", coefficient δ_1 corresponds to the contribution of the "$a \to b$" reaction step to the overall heat flow, coefficient δ_2 corresponds to the contribution of the whole reaction route "$a \to c \to d$" to the overall heat flow, and coefficient δ_3 is the share of the "$a \to c$" step in the heat flow produced within the reaction route "$a \to c \to d$".

The MKA optimization (see the solid lines in Fig. 4C) confirmed that this reaction scheme is correct and able to reproduce (although rather qualitatively, note $r^2 = 0.994$) the observed kinetics. From the mechanistic point of view the route I ($a \to b$) most probably represents the case when the actual decomposition reaction rate is the rate-determining step, i.e. oxygen is available at the $CaC_2O_4/CaCO_3$ reaction boundary to immediately oxidize the reaction-generated carbon monoxide. In such case the overall reaction is exothermic (due to the surplus evolved heat compared to the heat consumed by the endothermic decomposition) and it appears as a single step even though in reality it represents a consequent reaction (as

suggested in the pink-colored 4-step reaction scheme in Fig. 4). The second reaction route (a → c → d) then represents the case when diffusion of oxygen to the reaction boundary is the rate-determining step and the reaction route manifests itself as a true sequence of two following reactions (decomposition → oxidation). The competition between the two reaction routes is then driven via applied heating rate, which determines the conditions for oxygen diffusion to reaction boundary. This also indirectly implies that the decomposition reaction proceeds primarily from the grain volume (i.e. there is some diffusion layer present even at the start of the reaction).

As the full kinetics revelation of the DSC-measured decomposition reaction is beyond the scope of the present study (the MKA optimization was based on the qualitative curve-by-curve approach employing the Johnson-Mehl-Avrami kinetics as the model equation for all reaction steps), Fig. 4 further only lists several most promising reaction mechanisms (2 x 5-step and 1 x 6-step reactions) as proposed after closer examination of the DSC data (identification of small pre-peaks and shoulders on the main reaction peaks depicted in Fig. 4C). Further aspects to be considered during development of the improved reaction mechanism would certainly be: existence of multiple types of activation centers for the decomposition process (surface/volume defects), different crystal morphologies originating from the initial mixture of COM and COT crystallites, different degrees of material porosity associated with either 3 or 1 molecule of water being released from the respective COM and COT crystallite formulas).

5. Conclusions

Kinetics of dehydration and decomposition of oxalate trihydrate and monohydrate mixture was studied by means of DSC, TG and in-situ XRD. Šesták-Berggren equation was used to model the two consequent dehydration reactions. Good agreement was found between

the kinetic parameters calculated from the DSC and TG data – approximate values of activation energies were 68 and 81 kJ·mol^{-1} for the trihydrate→monohydrate and monohydrate→anhydride transformations, respectively. In case of the complex two-step dehydration process the DSC technique was found to provide the most precise and reliable data (compared to TG), especially at low temperatures and low heating rates. Hence this technique can be recommended for rigorous kinetic studies of oxalates dehydration. However, the enthalpy associated with the dehydration of the particular hydrates may depend on several factors and is generally not a most straightforward way to determine the representation of the particular types of oxalate hydrates, where thermogravimetry dominates. Contrary to the studies of amorphous→crystalline transitions, in case of the crystal→crystal transformations the in-situ XRD may be severely limited by the lack of well distinguished single diffraction lines corresponding to the reaction product of new polymorphic form created during physico-chemical transformation. It should be noted that in-situ XRD is also relatively time-consuming technique with limited magnitude of applicable heating rates; it would be therefore advantageous in case of very slow transformations, where DSC or TG signal would be lost in baseline noise. In case of the decomposition reaction kinetics the DSC provided more complex information, including the consequent oxidation reaction; however evaluation of the decomposition kinetics itself was therefore much more complicated. Thermogravimetry, on the other hand, provided very precise prediction of the single-step CaOx decomposition behavior; the corresponding activation energy was 180 kJ·mol^{-1}. In general, the use of a combination of different experimental techniques is a new trend in kinetics of solid state reactions [81 - 83]. Different techniques, such as TG, DSC or high temperature XRD, provide information about the processes from different perspectives and this complementary information is always very beneficial with regard to a more complete overview of the studied processes.

Regarding the kinetic calculations, the multivariate kinetic analysis was found to be very useful with respect to the solving of complex kinetic problems. It was demonstrated that the commonly used approach employing simultaneous optimization of all measured data-curves can be used only in case of perfectly aligned kinetic behavior (e.g. the TG decomposition data from the present study). In case of the kinetic behavior being inconsistent with respect to T or q^+, the averaged curve-by-curve approach needs to be adopted – merit of this approach is complete description and prediction of the trends in process kinetics; this approach is well suited for kinetic studies of oxalates dehydration studied either by DSC or TG. Nevertheless, the curve-by-curve optimization is applicable only in case of fully identified nature of process complexity – recommended practice in such case would be simultaneous optimization of 2 - 3 data-curves in order to reflect the trends in T/q^+-dependent kinetics and at the same time to allow for the proposed reaction mechanism to be fully tested.

Acknowledgments

This work was supported by the Czech Science Foundation under project no. 17-11753S.

References

[1] L.U. Ogbuji, C.D. Batich. Ultrastructure of whewellite kidney stones: electron-analytical investigation. J. Ultrastruct. Res. 90 (1985) 1-8.

[2] V. Tazzoli, C. Domeneghetti. The crystal structures of whewellite and weddellite: re-evaluation and comparison. Am. Mineral. 65 (1980) 327-324.

[3] F.J. Opalko, J.H. Adair, S.R. Khan. Heterogeneous nucleation of calcium oxalate trihydrate in artificial urine by constant composition J. Cryst. Growth 181 (1997) 410-417.

[4] C. Knoll, D. Muller, W. Artner, J.M. Welch, A. Werner, M. Harasek, P. Weinberger. Probing cycle stability and reversibility in thermochemical energy storage - CaC2O4_H2O as perfect match? Appl. Energ. 187 (2017) 1-9.

[5] S. Uma, J. Gopalakrishnan. K1-XLAXCA2-XNB3O10, A LAYERED PEROVSKITE SERIES WITH VARIABLE INTERLAYER CATION DENSITY, AND LACANB3O10, A NOVEL LAYERED PEROVSKITE OXIDE WITH NO INTERLAYER CATIONS. J. Solid State Chem. 102 (1993) 332-339.

[6] R.K. Sinha, S.K. Srivastava. FORMATION BEHAVIOR OF YBA2CU3O7-X-CONVENTIONAL PROCESSING. Supercond. Sci. Technol. 6 (1993) 238-245.

[7] I. Aboltina, R. Ramata, I. Brante. Chemically and thermally resistant lanthanoid bititanate ferroelectrics. Ferrolectrics 141 (1993) 277-285.
[8] A.K. Sharma, N.K. Kaushik. THERMAL STUDIES ON TITANYL AND ZIRCONYL OXALATES - A REVIEW. Thermochim. Acta 83 (1985) 347-376.
[9] V.B. Reddy, P.N. Mehrotra. IR AND THERMAL STUDIES ON LANTHANUM ZIRCONYL OXALATE J. Therm. Anal. 21 (1981) 21-26.
[10] B.C. Purukayastha, S.N. Bhattacharya. On the study of the use of calcium oxalate monohydrate in the investigation of rare earth and thorium activities. J. Inorg. Nucl. Chem. 10 (1959) 103-109.
[11] E.K. Girija, S.C. Latha, S.N. Kalkura, C. Subramanian, P. Ramasany. Crystallization and microhardness of calcium oxalate monohydrate. Mater. Chem. Phys. 52 (1998) 253-257.
[12] D.A. Schlusinger. Kidney Stone Disease: Say no to stones! Springer, Berlin, 2014, ISBN: 9783319121055.
[13] V.A. Finkielstein, D.S. Goldfarb. Strategies for preventing calcium oxalate stones. CMAJ 174 (2006) 1407-1409.
[14] Z. Jing, W. GuoZeng, J. Ning, Y. JiaWei, G. Yan, Y. Fang. Analysis of urinary calculi composition by infrared spectroscopy: A prospective study of 625 patients in Eastern China. Urol. Res. 38 (2010) 111-115.
[15] M. Daudon, R.J. Reveillaud. Whewellite and weddellite: toward a different etiopathogenesis. The significance of morphological typing of calculi Nephrologie 5 (1984) 195-201.
[16] M. Daudon, C.A. Bader, P. Jungers, W.G. Robertson, H.G. Tiselius, B. Hess, J.R. Asplin. Urinary calculi: Review of classification methods and correlations with etiology Scanning. Microsc. 7 (1993) 1081-1106.
[17] A. Hesse, W. D. Miersch. Special aspects of stone composition and aetiology of different types of urinary calculi. Int. Urol. Nephrol. 21 (1989) 257-260.
[18] F.S. Silvia, S.L. Silva, E.F. Daher, G.B. Silva Junior, R.M. Mota, C.A. Bruno da Silva. Determination of urinary stone composition based on stone morphology: a prospective study of 325 consecutive patients in an emerging country. Clin. Chem. Lab. Med. 47 (2009) 561–564.
[19] M. Liebman, I.A. Al-Wahsh. Probiotics and Other Key Determinants of Dietary Oxalate Absorption. Adv. Nutr. 2 (2011) 254-260.
[20] B. T. Murphy, L. N. Pyrah. The composition, structure and mechanisms of the formation of urinary calculi. J. Urol. 34 (1962) 129-159.
[21] J. R. Asplin, J. Lingeman, R. Kahnoski, H. Mardis, J. H. Parks, F. L. Coe. Metabolic urinary correlates of calcium oxalate dihydrate in renal stones. J. Urol. 159 (1998) 664-668.
[22] B.Q. Xie, TJ. Halter, B.M. Boran, G.H. Nancollas. Aggregation of Calcium Phosphate and Oxalate Phases in the Formation of Renal Stones Cryst. Growth Des. 15 (2015) 204-211.
[23] P. Vasquez-Quitral, J.T. Arana, M.C. Miras, D.F. Acevedo, C.A. Barbero, A. Neira-Carrillo. Effect of Diazotated Sulphonated Polystyrene Films on the Calcium Oxalate Crystallization. Crystals 7 (2017) 70:1-13.
[24] J. Chung, R. Sosa, J.D. Rimer. Elucidating the Effects of Polyprotic Acid Speciation in Calcium Oxalate Crystallization. Cryst. Growth Des. 17 (2017) 4280-4288.
[25] S. Li, W. Zhang, L. Wang. Direct Nanoscale Imaging of Calcium Oxalate Crystallization on Brushite Reveals the Mechanisms Underlying Stone Formation. Cryst. Growth Des. 15 (2015) 3038-3045.

[26] J.H. Chung, I. Granja, M.G. Taylor, G. Mpourmpakis, J.R. Asplin, J.D. Rimer. Molecular modifiers reveal a mechanism of pathological crystal growth inhibition. Nature 536 (2016) 446-+.
[27] T. Mandal, AG. Shtukenberg, A.C. Yu, X. Zhong, M.D. Ward. Effect of Urinary Macromolecules on L-Cystine crystal growth and crystal Surface Adhesion. Cryst. Growth Des. 16 (2016) 423-431.
[28] M. Zhang, X.H. Zhang, B. Zhang, D.W. Wang. Composition, microstructure and element study of urinary calculi. Microsc. Res. Tech. 79 (2016) 1038-1044.
[29] E. Akyol, K. Ongun, S. Kirboga, M. Oner. A kinetic study for Calcium Oxalate crystallization in the presence of Viburnum opulus extract. Biointerface Res. Appl. Chem. 6 (2016) 1064-1069.
[30] C.J. McMulkin, M. Massi, F. Jones. Calcium Oxalate crystal growth modification; investigations with confocal Raman microscopy. J. Cryst. Growth 468 (2017) 295-298.
[31] T.S. Jung, W.S. Kim, C.K. Choi. Biomineralization of calcium oxalate for controlling crystal structure and morphology. Mater. Sci. Eng. C24 (2004) 31–33.
[32] A.L. Rodgers, J. Garside. The nucleation and growth-kinetics of calcium-oxalate in the presence of some synthetic urine constituents. Investig. Urol. 18 (1981) 484–488.
[33] R. Selvaraju, J. Alli, S. Sulochana, M. Bhuwaneswari. DISSOLUTION STUDIES IN FEW URINARY TYPE CRYSTALS. J. Adv. Appl. Sci. Res. 1 (2017) SI -.
[34] M. Daudon, E. Letavernier, V. Frochot, J.P. Haymann, D. Bazin, P. Jungers. Respective influence of Calcium and Oxalate urine concentration on the formation of Calcium Oxalate monohydrate or dihydrate crystals. C. R. Chim. 19 (2016) 1504-1513.
[35] M.G. Hill, E. Konigsberger, P.M. May. Mineral precipitation and dissolution in the kidney. Am. Mineral. 102 (2017) 701-710.
[36] B. Tomažič, G.H. Nancollas. Kinetics of dissolution of calciumoxalate hydrates. J Cryst Growth 46 (1979) 355–361.
[37] J. Streit, L. Tran-Ho, E. Konigsberger. Solubility of the three calcium oxalate hydrates in sodium chloride solutions and urine-like liquors. Mon. Chem. 129 (1998) 1225–1236.
[38] G.L. Gardner. Nucleation and crystal growth of calcium oxalate trihydrate. J. Cryst. Growth 30 (1975) 158-168.
[39] D. Skrtic, M. Markovic, Lj. Komunjer, H. Furedi-Milhofer. Precipitation of calcium oxalates from high ionic strength solutions I. J. Cryst. Growth 66 (1984) 431-440.
[40] S. VeintemillasVerdaguer. Chemical aspects of the effect of impurities in crystal growth. Prog. Cryst. Growth. Ch. 32 (1996) 75-109.
[41] K. Pitt, G.P. Mitchell, A. Ray, B.R. Heywood, M.J. Hounslow. Micro-mechanical model of Calcium Oxalate monohydrate aggregation in supersaturated solutions: Effect of crystal form and seed concentration. J. Cryst. Growth 361 (2012) 176-188.
[42] E.P. Manche, B. Carroll. The kinetic isotope effect in dehydration of ionic solids 2. J. Phys. Chem. 81 (1977) 2637-2639.
[43] G. Sádovská, G. Wolf. Enthalpy of dissolution and thermal dehydration of calcium oxalate hydrates. J. Therm. Anal. Calorim. 119 (2015) 2063-2068.
[44] A. Kohutová, P. Honcová, V. Podzemná, P. Bezdička, E. Vecerniková, M. Louda, J. Seidel. Thermal analysis of kidney stones and their characterization. J. Therm. Anal. Calorim. 101 (2010) 695-699.
[45] T. Fei, X. Hao, S. Bao-Lian. A simultaneous thermal study in quantitaive analysis of calcium oxalate hydrates. Anal. Methods 5 (2013) 6900-6903.

[46] S. Ghosh, S. Basu, S. Chakraborty, A.K. Mukherjee. Structural and microstructural characterization of human kidney stones from eastern India using IR spectroscopy, scanning electron microscopy, thermal study and X-ray Rietveld analysis. J. Appl. Cryst. 42 (2009) 629-635.
[47] G. Madhurambal, N. Prabha, S.P. Lakshmi, S.C. Mojumdar. Thermal, UV, FTIR, and XRD studies of urinary stones. J. Therm. Anal. Calorim. 112 (2013) 1067-1075.
[48] Y. Masuda, Y. Ito, R. Ito, K. Iwata. Kinetic study of the thermal dehydration of calcium oxalate monohydrate. Thermochim. Acta 99 (1986) 205-215.
[49] S. Vyazovkin, A.K. Burnham, J.M. Criado, L.A. Pérez-Maqueda, C. Popescu, N. Sbirrazzuoli. ICATC Kinetics Committee recommendations for performing kinetic computations on thermal analysis data. Thermochim. Acta 520 (2011) 1–19.
[50] N. Kutaish, P. Aggarwal, D. Dollimore. Thermal analysis of calcium oxalate samples obtained by various preparative routes. Thermochim. Acta 297 (1997) 131-137.
[51] H.L. Anderson, A. Kemmler, G.W.H. Hohne, K. Heldt, R. Strey. Round robin test on the kinetic evaluation of a complex solid state reaction from 13 European laboratories. Part 1. Thermochim. Acta 332 (1999) 33-53.
[52] H.L. Anderson, A. Kemmler, R. Strey. Experiences with four software packages for kinetic evaluation in thermal analysis J. Therm. Anal. 47 (1996) 543-557.
[53] N. Eisenreich. Direct least squares fit of chemical reaction curves and its relation to the kinetic compensation effect. J. Therm. Anal. 19 (1980) 289-296.
[54] P.A. Bhatt, R.P. Laiya, D.B. Patil, P.V. Parikh, P. Paul. Analysis of the constituents of urinary calculi of dog using various scientific techniques. Curr. Sci. 110 (2016) 863-867.
[55] P. Honcová, R. Svoboda, P. Pilný, G. Sádovská, J. Barták, L. Beneš, D. Honc. Kinetic study of dehydration of calcium oxalate trihydrate. J. Therm. Anal. Calorim. 124 (2016) 151-158.
[56] P. Budrugeac, E. Segal. Non-isothermal kinetics of reactions whose activation energy depends on the degree of conversion. Thermochim. Acta 260 (1995) 75-85.
[57] Y. Nishikawa, K. Takahashi, Y. Masunari, M. Okabe, M. Yoshida, M. Ohota. Synthesis of calcium oxalate trihydrate crystal by homogeneous precipitation method and its structural analysis. J. Chem. Soc. Jpn. 7 (1994) 661-666.
[58] J. Kaloustian, A.M. Pauli, G. Pieroni, H. Portugal. The use of thermal analysis in determination of some urinary calculi of calcium oxalate. J. Therm. Anal. Calorim. 70 (2002) 959-973.
[59] J. Kaloustian, T.F. El-Moselhy, H. Portugal. Determination of calcium oxalate (mono- and dihydrate) in mixtures with magnesium ammonium phosphate or uric acid: the use of simultaneous thermal analysis in urinary calculi. Clin. Chim. Acta 334 (2003) 117-129.
[60] A.R. McGhie. Simultaneous thermogravimetry-differential thermal analysis-mass spectrometry (TG-DTA-MS) using a heated capillary interface. Thermochim. Acta 234 (1994) 21-29.
[61] R.L. Frost, M.L. Weier. Thermal treatment of whewellite – a thermal analysis and Raman spectroscopic study. Thermochim. Acta 409 (2004) 79-85.
[62] J. Šesták, Science of Heat and Thermophysical Studies: A Generalized Approach to Thermal Analysis, Elsevier, Amsterdam, 2005.
[63] H. E. Kissinger, Reaction kinetics in differential thermal analysis, Anal. Chem. 29 (1957) 1702-6.
[64] M. J. Starink, The determination of activation energy from linear heating rate experiments: a comparison of the accuracy of isoconversion methods, Thermochim. Acta 404 (2003) 163-76.

[65] J. Opfermann. Kinetic analysis using multivariate non-linear regression. J. Therm. Anal. Calorim. 60 (2000) 641-58.
[66] Tarasov AV, Tikhonov NA, Makarenko IV, Dunaev AV, Arhangelskii IV. Non-isothermal kinetic methods. Open Access Edition – Max Planck Research Library for the History and Development and Knowledge; 2013.
[67] S. Vyazovkin, A.K. Burnham, J.M. Criado, L.A. Pérez-Maqueda, C. Popescu, N. Sbirrazzuoli. ICATC Kinetics Committee recommendations for performing kinetic computations on thermal analysis data. Thermochim. Acta 520 (2011) 1–19.
[68] M. Avrami, Kinetics of phase change I – General theory, J. Chem. Phys. 7 (1939) 1103–1112.
[69] M. Avrami, Kinetics of phase change. II – Transformation-time relations for random distribution of nuclei, J. Chem. Phys. 7 (1940) 212–224.
[70] M. Avrami, Granulation, phase change, and microstructure – Kinetics of phase change III, J. Chem. Phys. 7 (1941) 177–184.
[71] D. Skrtic, M. Markovic, Lj. Komunjer, H. Furedi-Milhofer. Precipitation of calcium oxalates from ionic strength solutions I. J. Cryst. Growth 66 (1984) 431-440.
[72] JCPDS PDF-4+ database (2016) International Centre for Diffraction Data, Newtown Square, PA, U.S.A. release 2016.
[73] C. Conti, M. Casati, C. Colombo, E. Possenti, M. Realini, G.D. Gatta, M. Merlini, L. Brambilla, G. Zerbi. Synthesis of calcium oxalate trihydrate: New data by vibrational spectroscopy and synchrotron X-ray diffraction. Spectrochim. Acta A 150 (2015) 721-730.
[74] R.L. Frost, M.L. Weier. Thermal treatment of weddellite-a Raman and infrared emission spectroscopic study. Thermochim. Acta 406 (2003) 221-232.
[75] T.A. Shippey. Vibrational studies of calcium oxalate monohydrate (whewellite) and an anhydrous phase of calcium oxalate. J. Mol. Struct. 63 (1980) 157-166.
[76] D. Duval, R.A. Condrate. A Raman spectral study of the dehydration of calcium oxalate monohydrate. Appl. Spectrosc. 42 (1988) 701-703.
[77] D. Brandová, R. Svoboda, Z. Olmrová Zmrhalová, J. Chovanec, R. Bulánek, J. Romanová. Crystallization kinetics of glassy materials – the ultimate complexity? J. Therm. Anal. Calorim. – in press, https://doi.org/10.1007/s10973-018-7078-1.
[79] S. Gurrieri, G. Siracusa, R. Cali. Thermal decomposition of $CaC_2O_4.H_2O$: determination of kinetic parameters by DTG and DTA. J. Therm. Anal. 6 (1974) 293-298.
[80] A.M.M. Gadalla. Kinetics of the decomposition of hydrated oxalates of calcium and magnesium in air. Thermochim. Acta 74 (1984) 255-272.
[81] M. Fukuda, N. Koga, Kinetics and Mechanisms of the Thermal Decomposition of Copper(II) Hydroxide: A Consecutive Process Comprising Induction Period, Surface Reaction, and Phase Boundary-Controlled Reaction, J. Phys. Chem. C 122(24) (2018) 12869-12879.
[82] E. Gil-Gonzalez, A. Perejón, P.E. Sánchez-Jiménez, S. Medina-Carrasco, J. Kupčík, J. Šubrt, J.M. Criado, L.A. Pérez-Maqueda, Crystallization Kinetics of Nanocrystalline Materials by Combined X-ray Diffraction and Differential Scanning Calorimetry Experiments, Cryst. Growth Des. 18(5) (2018) 3107-3116.
[83] N. Koga, S. Kodani, Thermally induced carbonation of Ca(OH)2 in a CO2 atmosphere: Kinetic simulation of overlapping mass-loss and mass-gain processes in a solid-gas system, Phys. Chem. Chem. Phys. 20(41) (2018) 26173-26189.

Figure captions

Fig. 1: A) Example DSC (black), TG (red) and DTG (dashed blue) curves measured at heating rate of 5 °C·min^{-1} for the dehydration and consequent decomposition of prepared mixture of calcium oxalate hydrates (COT and COM).
B) XRD patterns obtained during in-situ heating scan at 30 °C (red patterns) and 90 °C (black pattern); the lower record represents overlap of both patterns for easier comparison.
C) Raman spectra obtained for as prepared material (red spectrum) and material heated in DSC to 90 °C (black spectrum). Inset shows zoomed 1420 – 1520 cm^{-1} region.
Lower right-side part of the figure displays schematic representations of Raman vibrations of the $C_2O_4^{2-}$ molecule and a SEM micrograph of as-prepared mixture of calcium oxalate hydrates.

Fig. 2: A) Full set of DSC signals corresponding to the dehydration of mixed calcium oxalate hydrates (COT and COM) measured at different q^+; inset shows measurements performed at lowest heating rates.
B) Black-based data (left and bottom axes) show Kissinger plots constructed from the DSC data depicted in Fig. 2A, empty points represent the low-temperature dehydration step (COT → COM), filled points represent the high-temperature dehydration step (COM → CaOx). Red-based data (right and top axes) show the E-α dependence obtained by means of the modified KAS method (points) and resulting E values from the Kissinger plot (red dashed lines).
C and D) Results from MKA calculations – points represent data from the curve-by-curve optimizations with fixed E values, dashed lines (of corresponding colors in graph D) represent the overall values obtained from a simultaneous MKA optimization of all DSC curves. Indices 1 and 2 correspond to the first (COT → COM) and second (COM → CaOx) dehydration steps.

Fig. 3: A) Full set of TG signals corresponding to the dehydration of mixed calcium oxalate hydrates (COT and COM) measured at different q^+; inset shows measurements performed at lowest heating rates.
B) Black-based data (left and bottom axes) show Kissinger plots constructed from the TG data depicted in Fig. 3A, empty points represent the low-temperature dehydration step (COT → COM), filled points represent the high-temperature dehydration step (COM → CaOx). Red-based data (right and top axes) show the E-α dependence obtained by means of the modified KAS method (points) and resulting E values from the Kissinger plot (red dashed lines).
C) Comparison of kinetic exponents for the two sub-processes, ratio coefficient I and correlation coefficient r^2 obtained from the DSC and TG data by the following two MKA approaches: simultaneous optimization of the whole dataset (denoted as "overall"), averaged results from curve-by-curve optimizations with fixed E values (denoted as "average").
D) Comparison of the degree of conversion α obtained from DSC, TG and in-situ XRD measurements performed at $q^+ = 0.5$ °C·min^{-1} and $q^+ = 20$ °C·min^{-1} (inset).

Fig. 4: A) Full set of TG signals corresponding to the decomposition of calcium oxalate (CaOx) measured at different q^+.

B) Black-based data (left and bottom axes) show Kissinger plot constructed from the TG data depicted in Fig. 4A. Red-based data (right and top axes) show the E-α dependence obtained by means of the modified KAS method (points) and resulting E value from the simultaneous MKA optimization (red dashed line).
C) Curve-by-curve MKA optimization of the DSC-measured joint CaOx decomposition and CO oxidation data obtained at higher heating rates. Points represent experimental data, lines show their best fit employing the reaction scheme displayed below with each reaction step being qualitatively modeled in accordance with JMA kinetics.
Lower right-side part of the figure displays further considered more advanced reaction schemes for the complex joint CaOx decomposition and CO oxidation processes – see text for details.

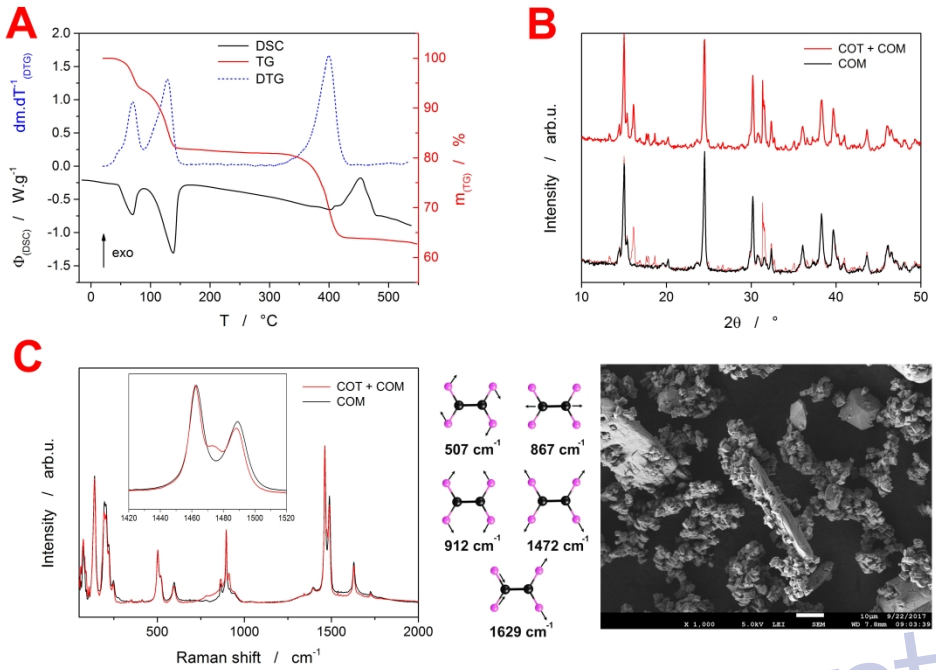

Fig. 1: A) Example DSC (black), TG (red) and DTG (dashed blue) curves measured at heating rate of 5 °C·min-1 for the dehydration and consequent decomposition of prepared mixture of calcium oxalate hydrates (COT and COM).
B) XRD patterns obtained during in-situ heating scan at 30 °C (red patterns) and 90 °C (black pattern); the lower record represents overlap of both patterns for easier comparison.
C) Raman spectra obtained for as prepared material (red spectrum) and material heated in DSC to 90 °C (black spectrum). Inset shows zoomed 1420 – 1520 cm-1 region.
Lower right-side part of the figure displays schematic representations of Raman vibrations of the C2O42- molecule and a SEM micrograph of as-prepared mixture of calcium oxalate hydrates.

579x399mm (300 x 300 DPI)

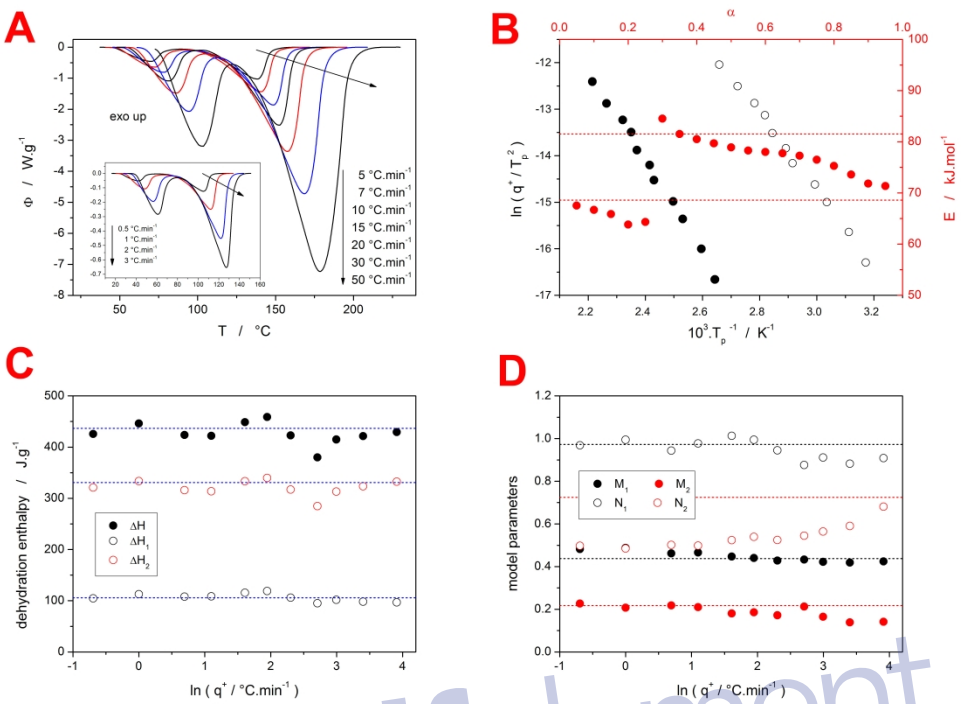

Fig. 2: A) Full set of DSC signals corresponding to the dehydration of mixed calcium oxalate hydrates (COT and COM) measured at different q+; inset shows measurements performed at lowest heating rates.
B) Black-based data (left and bottom axes) show Kissinger plots constructed from the DSC data depicted in Fig. 2A, empty points represent the low-temperature dehydration step (COT → COM), filled points represent the high-temperature dehydration step (COM → CaOx). Red-based data (right and top axes) show the E-α dependence obtained by means of the modified KAS method (points) and resulting E values from the Kissinger plot (red dashed lines).
C and D) Results from MKA calculations – points represent data from the curve-by-curve optimizations with fixed E values, dashed lines (of corresponding colors in graph D) represent the overall values obtained from a simultaneous MKA optimization of all DSC curves. Indices 1 and 2 correspond to the first (COT → COM) and second (COM → CaOx) dehydration steps.

590x420mm (300 x 300 DPI)

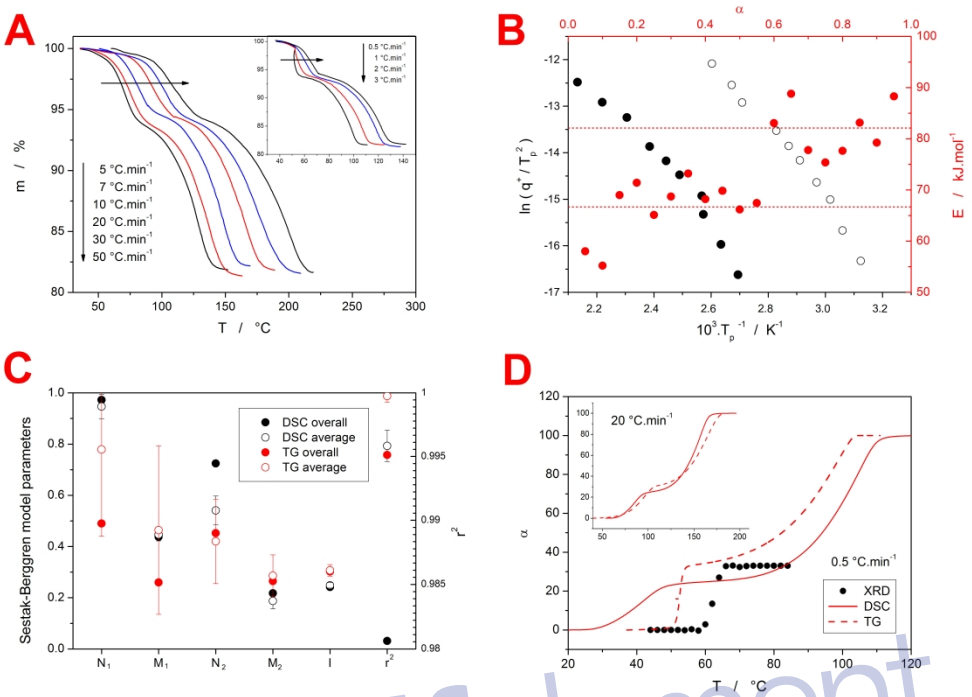

Fig. 3: A) Full set of TG signals corresponding to the dehydration of mixed calcium oxalate hydrates (COT and COM) measured at different q+; inset shows measurements performed at lowest heating rates.
B) Black-based data (left and bottom axes) show Kissinger plots constructed from the TG data depicted in Fig. 3A, empty points represent the low-temperature dehydration step (COT → COM), filled points represent the high-temperature dehydration step (COM → CaOx). Red-based data (right and top axes) show the E-α dependence obtained by means of the modified KAS method (points) and resulting E values from the Kissinger plot (red dashed lines).
C) Comparison of kinetic exponents for the two sub-processes, ratio coefficient I and correlation coefficient r2 obtained from the DSC and TG data by the following two MKA approaches: simultaneous optimization of the whole dataset (denoted as "overall"), averaged results from curve-by-curve optimizations with fixed E values (denoted as "average").
D) Comparison of the degree of conversion α obtained from DSC, TG and in-situ XRD measurements performed at q+ = 0.5 °C·min-1 and q+ = 20 °C·min-1 (inset).

590x420mm (300 x 300 DPI)

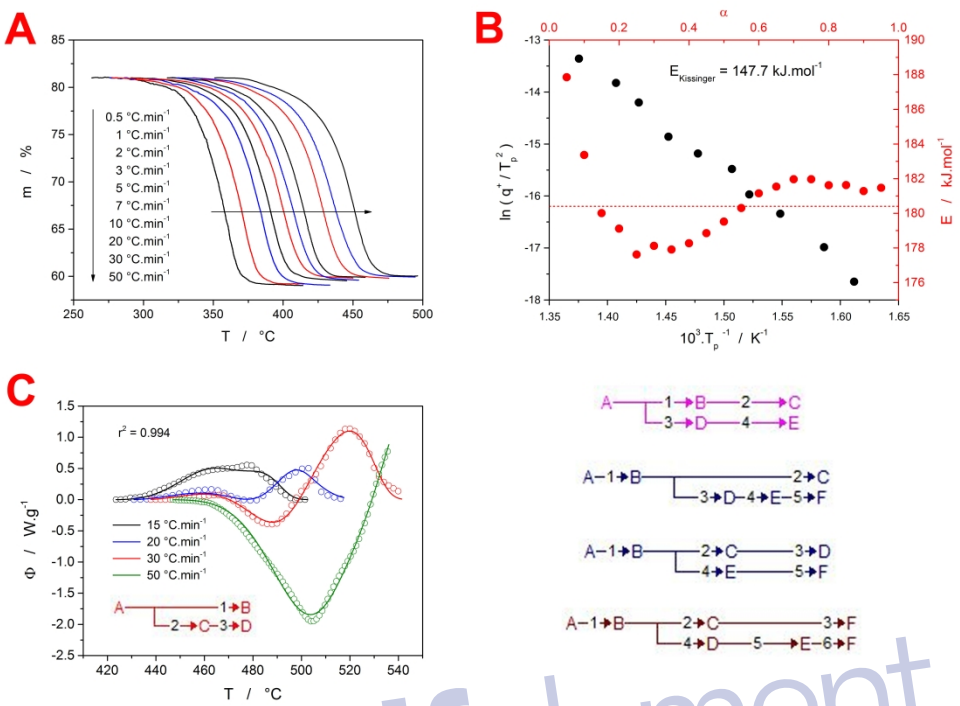

Fig. 4: A) Full set of TG signals corresponding to the decomposition of calcium oxalate (CaOx) measured at different q+.
B) Black-based data (left and bottom axes) show Kissinger plot constructed from the TG data depicted in Fig. 4A. Red-based data (right and top axes) show the E-α dependence obtained by means of the modified KAS method (points) and resulting E value from the simultaneous MKA optimization (red dashed line).
C) Curve-by-curve MKA optimization of the DSC-measured joint CaOx decomposition and CO oxidation data obtained at higher heating rates. Points represent experimental data, lines show their best fit employing the reaction scheme displayed below with each reaction step being qualitatively modeled in accordance with JMA kinetics.
Lower right-side part of the figure displays further considered more advanced reaction schemes for the complex joint CaOx decomposition and CO oxidation processes – see text for details.

579x420mm (300 x 300 DPI)

Whereas thermogravimetry monitors only single-step CaOx decomposition reaction, DSC in addition reveals the complex competing CO oxidation kinetics.

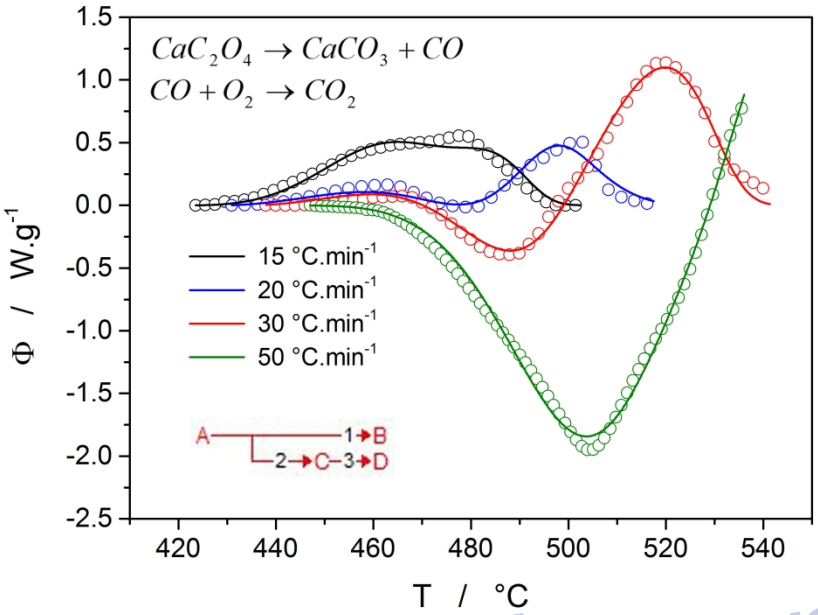

288x201mm (300 x 300 DPI)